




Internal photoemission spectroscopy determination of barrier heights between Ta-based amorphous metals and atomic layer deposited insulators

Cite as: J. Appl. Phys. 125, 055301 (2019); <https://doi.org/10.1063/1.5066569>

Submitted: 15 October 2018 . Accepted: 09 January 2019 . Published Online: 01 February 2019

M. A. Jenkins , J. M. McGlone, J. F. Wager , and J. F. Conley 



View Online



Export Citation



CrossMark

Ultra High Performance SDD Detectors



See all our XRF Solutions

Internal photoemission spectroscopy determination of barrier heights between Ta-based amorphous metals and atomic layer deposited insulators

Cite as: J. Appl. Phys. 125, 055301 (2019); doi: 10.1063/1.5066569

Submitted: 15 October 2018 · Accepted: 9 January 2019 ·

Published Online: 1 February 2019




View Online



Export Citation



CrossMark

M. A. Jenkins,  J. M. McClone, J. F. Wager,  and J. F. Conley, Jr. ^{a)} 

AFFILIATIONS

School of Electrical Engineering and Computer Science, Oregon State University, Corvallis, Oregon 97330, USA

^{a)} Author to whom correspondence should be addressed: jconley@eecs.oregonstate.edu

ABSTRACT

The energy barrier heights between two recently reported Ta-based amorphous metals (TaWSi and TaNiSi), TaN, and atomic layer deposited Al_2O_3 and HfO_2 insulators are measured in metal/insulator/metal (MIM) structures with Au top electrodes using internal photoemission (IPE) spectroscopy. For Al_2O_3 , the Ta-based metal barrier heights, φ_{Bn} , increase with increasing metal work function, Φ_{M} , for TaN, TaWSi, and TaNiSi, respectively. For HfO_2 , however, the barrier heights are relatively constant for all three metals $\varphi_{\text{Bn,TaNiSi}} \approx \varphi_{\text{Bn,TaWSi}} \approx \varphi_{\text{Bn,TaN}}$. The difference between HfO_2 and Al_2O_3 is attributed to enhanced Fermi-level pinning due to a larger dielectric constant. The slope parameter, S , was found to be roughly 0.89 and 0.44–0.69 for Al_2O_3 and HfO_2 , respectively. For devices with a TaWSi bottom electrode, a comparison was also made between Al and Au top electrodes. Significantly, smaller barrier heights were obtained with an Au top electrode than with an Al top electrode, 0.6 eV and 0.8 eV lower for HfO_2 and Al_2O_3 , respectively. IPE energy barriers are found consistent with current-voltage asymmetry of MIM diodes, whereas Schottky model predictions of barrier heights were inconsistent.

Published under license by AIP Publishing. <https://doi.org/10.1063/1.5066569>

I. INTRODUCTION

Metal-insulator-metal (MIM) and dual-insulator MIM (MIIM) structures are used in rectifying antennas (rectennas) for infrared energy harvesting,^{1–3} hot-electron transistors,^{4,5} single electron transistors,⁶ resistive random access memory (RRAM),⁷ and capacitors.^{8,9} These devices require the use of a smooth bottom electrode in order to produce a uniform electric field across the ultra-thin sandwiched insulator(s).^{10,11} ZrCuAlNi, an ultrasmooth amorphous metal, has seen use as the bottom electrode in MIM devices,^{10,12,13} however, it is limited by the presence of a ZrO_x interfacial layer, a relatively low effective work function near that of aluminum,¹⁴ and most significantly, a low thermal stability limited to less than about 400 °C.^{12,14} TaWSi and TaNiSi are two alternative amorphous metals that show much greater thermal stability, up to 900 °C for TaWSi and 600–700 °C for TaNiSi, and are expected to have minimal interfacial oxides.^{15,16} Based on the vacuum

work functions of their constituent elements, both TaWSi and TaNiSi are expected to have larger effective work functions than ZrCuAlNi and are thus more desirable as electrodes for these applications.

Precise knowledge of metal/insulator barrier heights, φ_{Bn} , is critical for predicting, understanding, and optimizing MIM device charge transport and operation.¹⁷ In the simplest model, charge transfer across the interface is neglected, and φ_{Bn} should vary with the vacuum work function of the metal, $\Phi_{\text{M,vac}}$, so that $\varphi_{\text{Bn}} = \Phi_{\text{M,vac}} - \chi_{\text{i}}$, where χ_{i} is the insulator electron affinity. However, this is not typically the case.^{17,18} In the metal induced gap state (MIGS) theory, charge transfer at intrinsic interface traps creates an interfacial dipole that drives the metal Fermi level, E_{Fm} , toward the charge neutral level of the insulator, $E_{\text{CNL,i}}$, the energy at which the dominant character of the interface states in the forbidden gap switches from donor-like to acceptor-like.^{19,20} Thus, the metal behaves

as if it has an effective work function, $\Phi_{M,eff}$, different from $\Phi_{M,vac}$, where

$$\Phi_{M,eff} = E_{CNL,i} + S(\Phi_{M,vac} - E_{CNL,i}), \quad (1)$$

where S is the slope of a plot of φ_{Bn} versus $\Phi_{M,vac}$ for a given insulator²¹

$$S = \frac{\partial \varphi_{Bn}}{\partial \Phi_M}. \quad (2)$$

S describes how much $\Phi_{M,eff}$ actually changes in response to a change in $\Phi_{M,vac}$, where $S = 0$ indicates complete “pinning” of E_{Fm} at $E_{CNL,i}$ and $S = 1$ indicates an absence of pinning.

Despite good success of this theory, it is difficult to calculate or determine the E_{CNL} for a given material and it is often observed that φ_{Bn} 's can deviate substantially from predictions due to extrinsic defects that can arise from processing details such as the deposition method, interface traps and near interfacial trapped charge due to point defects, dipoles due to interfacial chemical reactions, and remote scavenging of oxygen. It is therefore necessary to directly measure φ_{Bn} for each metal/insulator combination.

An electro-optical technique that allows for the direct measurement of specific interfacial energy barriers within a device structure is internal photoemission (IPE) spectroscopy.¹⁷ Although IPE has been widely used to characterize the interfaces between various polycrystalline elemental metals and oxides within MOS structures,^{18,22,23} there have been only a few reports of IPE within MIM structures,^{17,24–27} and only one previous report of IPE on an amorphous electrode.¹⁴

In this work, we use IPE spectroscopy to directly measure barrier heights in MIM device structures between two new Ta-based amorphous metals (TaNiSi and TaWSi), TaN, and insulators (Al_2O_3 and HfO_2) deposited via atomic layer deposition (ALD).

II. EXPERIMENTAL

MIM devices were fabricated on Si substrates with 100 nm of thermally grown SiO_2 to provide electrical isolation from the underlying Si. TaWSi and TaNiSi bottom electrodes were deposited using DC magnetron sputtering from single alloy targets targeting a thickness of 100 nm, verified via profilometry.^{15,16} TaN bottom electrode substrates (obtained from ON Semiconductor, Gresham, OR) consisted of a Si/ SiO_2 /Ta/TaN stack that was planarized via chemical mechanical polishing. Insulators were deposited on the bottom electrodes using atomic layer deposition (ALD), targeting a thickness of roughly 15 nm, such that the insulator was thick enough to prevent direct tunneling from dominating charge transport. Al_2O_3 and HfO_2 were deposited using thermal ALD in a Picosun SUNALE R-150 reactor at 250 °C. The precursors used for Al_2O_3 and HfO_2 were trimethylaluminum (TMA) and tetrakis(ethylmethylamino)hafnium (TEMA-Hf), respectively, with H_2O as the oxidizing agent. Insulator thickness was monitored by including a Si witness wafer (with a ~1.2 nm

layer of native SiO_2) in the ALD chamber for each deposition. For the semi-transparent top contact needed for IPE measurements, approximately 10 nm of either Al or Au was deposited via thermal evaporation, monitored with a quartz crystal microbalance. Au top electrodes were patterned with a shadow mask to yield circular devices with a diameter of 250 μm . Al top electrodes were patterned with photolithography into 200 by 200 μm squares. No anneals were performed.

IPE measurements were conducted using a 150 W Xe arc lamp source that was passed through a monochromator and then a long-pass filter (to remove second-order diffraction). The light was then shined onto the device of interest using a parabolic mirror focused to a spot size of 1 mm². Electrical bias was applied to the MIM bottom electrode and the top electrode was held at ground. At each applied bias, V , the electrical current was measured as the photon energy ($h\nu$) was swept from 2 to 5 eV (620–248 nm). A large increase in current is detected as $h\nu$ approaches the height of the electron energy barrier between the metal and the insulator. The current was normalized by subtracting the dark current for each applied bias, such that only photo-induced current was analyzed. The quantum yield, Y , was calculated from normalized current, and spectral thresholds, φ_{thresh} , the photon energy at which photo-induced current exceeds the dark current for a given applied bias, were determined from plots of $Y^{1/2}$ versus $h\nu$.^{18,28} To determine φ_{thresh} for each applied bias, an algorithm was implemented to find the largest region of the $Y^{1/2}$ curve with the highest linearity, as determined from the R^2 value of a linear regression. A linear regression of this region intercepted with the baseline gives φ_{thresh} for that specific bias. The zero-field barrier height, φ_{Bn} , for each interface was then found as the y-intercept of a Schottky plot of φ_{thresh} vs. the square root of the field across the insulator, $\xi^{1/2}$. The $\xi^{1/2}$ values are corrected for the built-in field, ξ_{bi} , of each device (taken as the field at which emission switches from the top to the bottom electrode). Reported φ_{Bn} values have an estimated accuracy of ± 0.1 eV. This is in line with commonly reported error values ranging from 0.05 to 0.1 eV.²⁹

III. RESULTS AND DISCUSSION

Shown in Fig. 1 are representative yield plots of $Y^{1/2}$ vs. $h\nu$ taken at various applied biases ranging between 0.4 and 1.2 MV²/cm² for (a) Al_2O_3 and (b) HfO_2 insulators in Au top electrode MIM devices with TaN, TaNiSi, or TaWSi bottom electrodes. The dashed lines indicate the linear regressions that were used to determine the φ_{thresh} .

Next, to determine whether image force barrier lowering is present, Schottky plots of the φ_{thresh} values vs. $\xi^{1/2}$ for the MIM devices from (a) and (b) are shown in (c) and (d) for Al_2O_3 and HfO_2 insulators, respectively, under both positive and negative ξ . The zero-field barrier heights for the Au interfaces (φ_{Bn-Au}) and the Ta-based metal interfaces (φ_{Bn-TaX}) were determined from the y-axis intersection of extrapolated linear fits of the φ_{thresh} 's. φ_{Bn} 's and top-bottom barrier differences ($\Delta\varphi_{Bn}$) for each insulator are listed in Table I. Although the

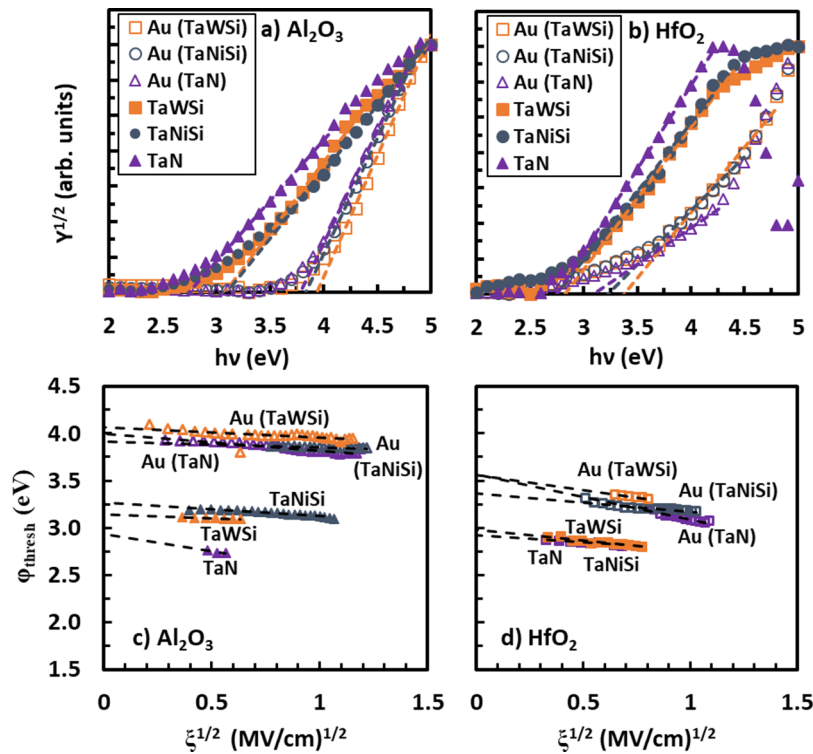


FIG. 1. Representative plots of $Y^{1/2}$ vs. $h\nu$ for (a) Al_2O_3 and (b) HfO_2 in MIM devices with Au top electrodes and with either a TaN, TaWSi, or TaNiSi bottom electrode as indicated. The dashed lines show the linear φ_{thresh} extraction for each interface. Also shown are Schottky plots of φ_{thresh} vs. $\xi^{1/2}$ used to extrapolate the φ_{Bn} from IPE-derived φ_{thresh} values for (c) Al_2O_3 and (d) HfO_2 .

φ_{thresh} values are field dependent, the slopes of the Schottky plots do not correlate with the insulator dielectric constant for any of the devices tested. An absence of image-force barrier lowering for IPE measurements is not unusual and has previously been reported in IPE of metal-insulator interfaces, where it was attributed to interfacial charge or to the presence of an interfacial layer.^{24,30–32} A plane of charge located near the injecting interface can effectively “pin” the top of the barrier reducing the influence of electric field on the barrier height.¹⁸ Likewise, a higher κ interfacial oxide at the injecting interface can also reduce expected electric field lowering.²⁹

TABLE I. Barrier heights extracted from devices with Au top electrodes, compared to literature values for the respective Au barrier height. Measured barrier heights are given with an expected error of ± 0.1 eV. Electron affinities from the literature are provided.

Insulator (χ_i)	Measured φ_{Bn} (± 0.1 eV)				Literature $\varphi_{\text{Bn,Au}}$ (eV)
	TaN	TaWSi	TaNiSi	Au (TaN, TaWSi, TaNiSi)	
Al_2O_3 (1.4 eV ³⁴)	2.9	3.1	3.3	4.0, 4.1, 3.9	4.1 ³⁰
HfO_2 (2.25 eV ³⁵)	2.9	3.0	3.0	3.5, 3.5, 3.4	3.7 ³¹

Note that there are two non-idealities that can be seen in the yield curves in (a) and (b). First, the yield curves for the barrier between HfO_2 and the top electrode show “tailing” at photon energies below the spectral threshold. This has been reported previously and may be attributed to conduction band tailing or charge in the HfO_2 .^{14,30} Second, the low positive bias yield curves (emission from the bottom electrode) for HfO_2 shows a rollover at high photon energies that appears most prominently with TaN bottom electrodes. This was also seen in our previous report of SiO_2 devices with the same electrodes.³³ The rollover becomes less prominent with increasing applied positive bias. It is likely that this rollover at high photon energy is due to photoelectron emission from the top Au electrode overwhelming emission from the bottom TaN electrode when there is a low positive bias/weak field across the insulator. At higher positive biases, the insulator field will repel photoelectrons back into the Au electrode. The reasons for stronger emission from the Au electrode at large photon energy are (i) photon absorption and thus photoelectron generation in the top electrode is much stronger than in the bottom electrode and (ii) the Au barrier heights are larger than the TaN barrier heights so that photoemission over the Au/insulator barrier does not start until higher photon energies.

Energy band diagrams based on the experimentally determined φ_{Bn} values listed in Table I are shown in Fig. 2. There are several interesting aspects of these results. At the top electrode, the Au/insulator barrier heights are consistent for each insulator (within the ± 0.1 eV error), regardless of the bottom electrode used. Additionally, the $\varphi_{\text{Bn,Au}}$ value of ~ 4.0 eV for Al_2O_3 is roughly consistent with the ideal Schottky model prediction ($\varphi_{\text{Bn,Au-ideal}} = \Phi_{\text{M}} - \chi_1$) given $\Phi_{\text{Au}} \sim 5.2$ eV and $\chi_{\text{Al}_2\text{O}_3} \sim 1.4$.³⁴ The $\varphi_{\text{Bn,Au}}$ of ~ 3.5 eV for HfO_2 , however, is higher than expected from the ideal theory prediction by about 1.1 eV.³⁵ φ_{Bn} values for both Au barriers are roughly consistent with previous IPE reports.

Considering next the Ta-based metal bottom electrodes, previous Kelvin probe work with TaWSi has determined $\Phi_{\text{TaWSi}} = 5.06$ eV.³⁶ Based on the average vacuum work functions of the constituent metals, it is expected that TaNiSi should have larger barrier heights than TaWSi which in turn should have larger barrier heights than TaN. This expected relative trend of $\varphi_{\text{Bn,TaNiSi}} > \varphi_{\text{Bn,TaWSi}} > \varphi_{\text{Bn,TaN}}$ is indeed observed for Al_2O_3 . For HfO_2 , however, the barrier heights are essentially the same for all three metals ($\varphi_{\text{Bn,TaNiSi}} \approx \varphi_{\text{Bn,TaWSi}} \approx \varphi_{\text{Bn,TaN}}$). Prior IPE work also appears to show a lack of a trend between various Φ_{M} metals and $\varphi_{\text{Bn,M/HfO}_2}$.¹⁸

The insensitivity of the HfO_2 barrier heights to the various metals suggests that a strong degree of E_{Fm} pinning at E_{CNL} is likely occurring at the HfO_2 interfaces. To quantify the degree of pinning, the slope parameter, S , from Eq. (2) is determined from the plots of φ_{Bn} versus $\Phi_{\text{M,vac}}$ (Au, Al, and TaWSi) shown in Figs. 3(a) for HfO_2 and 3(b) for Al_2O_3 . For HfO_2 , considering

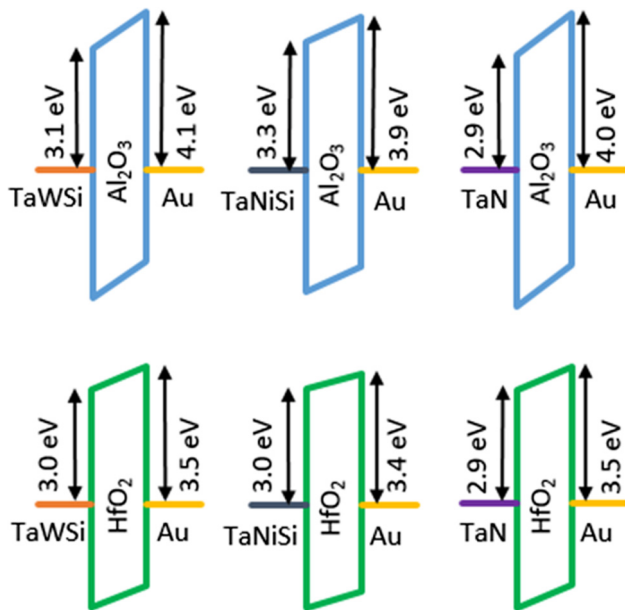


FIG. 2. IPE based energy band diagrams for Al_2O_3 and HfO_2 MIM devices with Au top electrodes and TaWSi, TaNiSi, or TaN bottom electrodes as indicated.

the experimental error, an S_{HfO_2} range roughly between 0.44 and 0.69 is found with $S_{\text{HfO}_2} = 0.56$ giving the best fit and shown by the dashed line in 3(a). This value is consistent with the 0.53 calculated by Robertson³⁷ as well as reported experimental values of around 0.5.^{21,38} While the $S_{\text{Al}_2\text{O}_3} = 0.89$ determined from 3(b) is considerably higher than the calculated value of 0.63,³⁷ it is in reasonably good agreement with the 0.83 value reported based on more recently measured IPE barrier heights from the literature.¹⁸

According to Mönch,²⁰ S may also be correlated with the high-frequency dielectric constant (ϵ_{∞}) of an insulator as

$$S = \frac{1}{1 + 0.1(\epsilon_{\infty-1})^2}. \quad (3)$$

This empirical relation reveals that as ϵ_{∞} increases, S decreases indicating that E_{Fm} is more effectively pinned at

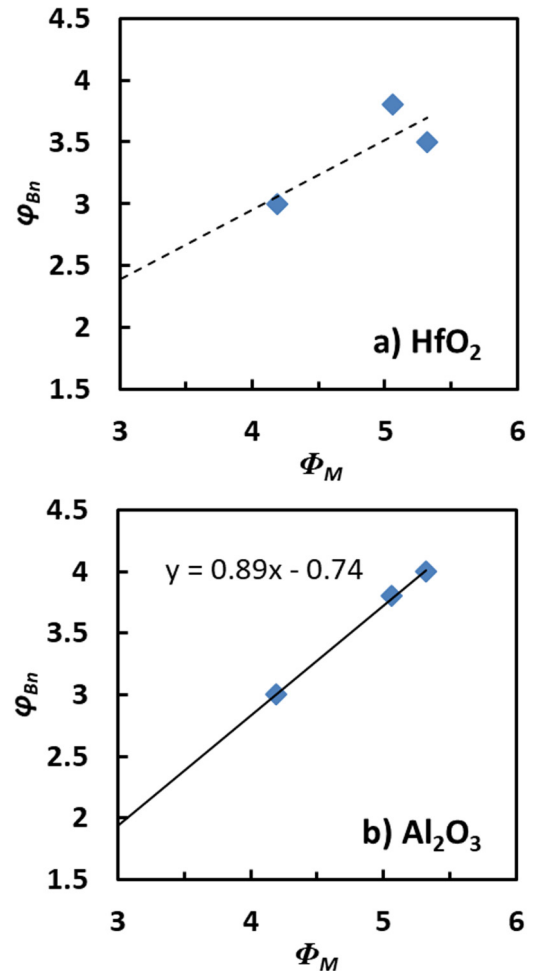


FIG. 3. Plots of φ_{Bn} vs. Φ_{M} (Al, Au, and TaWSi) for (a) HfO_2 and (b) Al_2O_3 .

$E_{\text{CNL},i}$. The fact that $\epsilon_{\infty,\text{HfO}_2} > \epsilon_{\infty,\text{Al}_2\text{O}_3}$ explains in part why $S_{\text{HfO}_2} < S_{\text{Al}_2\text{O}_3}$ and why barrier heights on HfO_2 are relatively independent of $\Phi_{\text{M,vac}}$. As ϵ_{∞} is also influenced by film morphology and crystallographic direction, it is likely that much of the difference between the theoretical calculation of the S parameter for Al_2O_3 and the value found in this work is because the calculations were performed for crystalline Al_2O_3 , which has a higher dielectric constant than the thin film amorphous Al_2O_3 deposited in this work. Using S values determined in this work and Eq. (3) yields $\epsilon_{\infty,\text{HfO}_2} = 3.8$ and $\epsilon_{\infty,\text{Al}_2\text{O}_3} = 2.1$. These values are both slightly lower than the range of 4.2–4.5 for HfO_2 and 2.5–3.0 for Al_2O_3 that were estimated from the square of the ellipsometric refractive index (RI^2) for similarly deposited materials,⁹ and may point to the presence of low κ interfacial layer at the Ta-based metal interface.³⁸

Since we are directly measuring φ_{Bn} , rather than $\Phi_{\text{M,eff}}$, Eq. (1) can be rewritten as³⁹

$$\varphi_{\text{Bn}} = S\Phi_{\text{M,vac}} - [\chi_1 - E_{\text{CNL}}(1 - S)], \quad (4)$$

assuming that the E_{CNL} is referenced to the vacuum level, E_{vac} , rather than the insulator valence band edge, E_v . By finding the y-intercept of a linear regression of the data in Fig. 3 and assuming $\chi_{\text{HfO}_2} = 2.25$ eV³⁵ and $\chi_{\text{Al}_2\text{O}_3} = 1.4$ eV,³⁴ we roughly estimate $E_{\text{CNL-vac,HfO}_2} = 6.3 - 7.6$ eV and $E_{\text{CNL-vac,Al}_2\text{O}_3} = 6.2$ eV, both referenced to E_{vac} . Assuming $E_{\text{G,HfO}_2} = 5.6$ eV and $E_{\text{G,Al}_2\text{O}_3} = 6.4$ eV,⁹ typical values for ALD films, this translates to a rough estimate of $E_{\text{CNL-v,HfO}_2} = 0.25 - 1.6$ eV and $E_{\text{CNL-v,Al}_2\text{O}_3} = 1.6$ eV, referenced to E_v . Robertson calculated $E_{\text{CNL-v}}$ values of 3.7 and 5.5 eV for HfO_2 and Al_2O_3 , respectively.³⁷ Using $\Phi_{\text{M,eff}}$ values extracted from flatband voltage shifts of capacitance-voltage measurements on arrays of MOS structures, Yeo *et al.*²¹ reported experimental E_{CNL} values of 3.64 and 6.62 eV for HfO_2 and Al_2O_3 , respectively, while Samavedam *et al.*³⁸ reported values of 4.5 and 5.2 eV for HfO_2 and Al_2O_3 , respectively, all referenced to E_v . Clearly the E_{CNL} values determined here are significantly lower than the previous reports. It is important to note that the calculations were performed for crystalline systems,³⁷ where the ALD thin films in this work are amorphous. In addition, all of the previous reports assume the crystalline $E_{\text{G,Al}_2\text{O}_3} = 8.8$ eV, which is much larger than the 6.4 eV measured by reflection electron energy loss spectroscopy (REELS) for similarly deposited unannealed ALD Al_2O_3 used in this work and the 6.4–6.9 eV values typically reported for unannealed ALD Al_2O_3 .^{9,40} For example, the $E_{\text{CNL,Al}_2\text{O}_3} = 6.62$ eV reported by Yeo *et al.* would be above the conduction band of ALD Al_2O_3 . The discrepancy between the E_{CNL} values in this work and previously reported values is likely attributable to extrinsic effects. Whereas the MIGS model described by Eq. (1) is based entirely on ideal intrinsic induced interface states, barrier heights in real devices may be heavily influenced by extrinsic effects due to processing, etc., such as interface trap point defects,⁴¹ additional dipoles due to interfacial chemical reactions, interface layer formation, trapped charge in the dielectric near the interface, and remote oxygen scavenging from the opposing metal electrode.⁴² In this work,

no post-deposition anneal is performed. In addition, MIM rather than MOS structures were used.

The absolute magnitudes of the extracted barrier heights for the Ta-based metals are much lower than predicted by the ideal model ($\varphi_{\text{Bn-ideal}} = \Phi_{\text{M}} - \chi_1$) based on their vacuum metal work functions. Two possible explanations to consider for the reduced barriers are hole emission and charge in the dielectric.

Although there are no reports of experimental IPE of holes from a metal into an insulator with a barrier above 2 eV,^{29,43} it is worth considering whether the lower than expected barrier measurements might be explained instead by hole emission from the Au electrode rather than electron emission from the bottom electrode. If this were the case, the measured barrier height would correspond to the Au/insulator hole barrier height ($\varphi_{\text{Bp,Au/HfO}_2}$) rather than the TaWSi/insulator electron barrier height. Considering first HfO_2 , the bandgap of HfO_2 should be equal to the sum of the electron and hole barriers: $E_{\text{G,HfO}_2} = \varphi_{\text{Bn,Au/HfO}_2} + \varphi_{\text{Bp,Au/HfO}_2}$. The $\varphi_{\text{Bn,Au/HfO}_2}$ measured is 3.5 eV (close to the 3.7 eV reported in Ref. 30). The E_{G} for these films was measured to be 5.6 eV via REELS,⁹ consistent with other reports for ALD HfO_2 . Thus, the expected $\varphi_{\text{Bp,Au/HfO}_2} = E_{\text{G,HfO}_2} - \varphi_{\text{Bn,Au/HfO}_2} = 5.6$ eV $-$ 3.5 eV = 2.2 eV. This is well below the $\varphi_{\text{Bn,TaWSi/HfO}_2} = 3.0$ eV barrier measured in Fig. 1, evidence that the measured HfO_2 barrier is indeed due to electrons rather than holes. For Al_2O_3 , $E_{\text{G,Al}_2\text{O}_3} = \varphi_{\text{Bn,Au/Al}_2\text{O}_3} + \varphi_{\text{Bp,Au/Al}_2\text{O}_3}$. The measured $\varphi_{\text{Bn,Au/Al}_2\text{O}_3} = 4.1$ eV \pm 0.1 eV. The E_{G} for these films was measured via REELS to be 6.4 eV,⁹ consistent with other reports for ALD Al_2O_3 .³⁰ Thus, the expected $\varphi_{\text{Bp,Au/Al}_2\text{O}_3} = E_{\text{G,Al}_2\text{O}_3} - \varphi_{\text{Bn,Au/Al}_2\text{O}_3} = 6.4$ eV $-$ 4.1 eV = 2.3 eV. This is well below the $\varphi_{\text{Bn,TaWSi/Al}_2\text{O}_3} = 3.1$ eV barrier measured in Fig. 1, evidence that the measured Al_2O_3 barrier is also due to electrons rather than holes.

Considering the oxide charge, previous work with Ta-based metals postulated that negative Ta ion migration into the oxide following a post-deposition anneal could lead to an increase in the barrier height.⁴⁴ While Ta diffusion could be playing a role, barrier heights here are reduced, rather than increased. Previous work has also shown that hole trapping ($\sim 10^{12}/\text{cm}^2$) can result in a local reduction of the barrier height by 0.3 eV, and Li^+ ions ($\sim 10^{14}/\text{cm}^2$) can reduce barrier heights by up to 1 eV.²⁹ Positively charged Au^+ ions are known to migrate rapidly through oxides and have even been shown to form conductive bridges that enable switching behavior in conductive bridging random access memory (CBRAM).^{45,46} Determination of the bottom electrode barrier heights in this work is performed with a positive bias applied to the Au top electrodes over a relatively long period of time (hours compared to less than a second for CBRAM devices), giving ample time for Au^+ ions to drift to the bottom electrode where they would contribute to a reduction in the barrier height. In fact, in support of this possibility, we have observed reversible breakdown/resistive switching behavior in the Au/ SiO_2 /TaWSi devices, whereas the Al/ SiO_2 /TaWSi devices did not show switching.³³

To assess whether Au may be impacting the extracted barrier heights of the opposing Ta-based electrodes, Al was

used as a top electrode for devices with a TaWSi bottom electrode and either Al_2O_3 or HfO_2 . Shown in Fig. 4 are representative yield plots of $Y^{1/2}$ vs. $h\nu$ for Al top electrode MIM devices with (a) Al_2O_3 and (b) HfO_2 insulators and TaWSi bottom electrodes. Schottky plots of the φ_{thresh} values vs. $\xi^{1/2}$ for these devices are shown in (c). Note that the yield curve for the HfO_2 barriers in (b) shows tailing at photon energies below the indicated spectral threshold and, as is typically reported for IPE of metal/insulator interfaces, the slopes of the Schottky plot of electric field barrier lowering in (c) do not correspond to the dielectric constant of the insulator.²⁹ Both of these observations are consistent with our previous IPE measurements on ZrCuAlNi amorphous metal bottom electrode/Al top electrode devices¹⁴ and have been attributed to either conduction band tailing/defects, charged defect levels, or an interfacial layer (IL) oxide at the injecting interface.^{24,30–32} Conduction band tailing is likely not solely responsible for the observed IPE threshold tailing as the energy spread of the tail is about 1 eV, larger than what would be typically expected for band tailing, though oxygen vacancy related defects have been detected using REELS at roughly 2 eV above the valance band edge in Ar^+ sputtered HfO_2 .⁹ Potential contributions from ILs would be either an Al_2O_3 IL at the top Al interface and a TaO_x IL at the Ta-based metal interface.⁴⁷ Given that the tailing was also seen with Al top

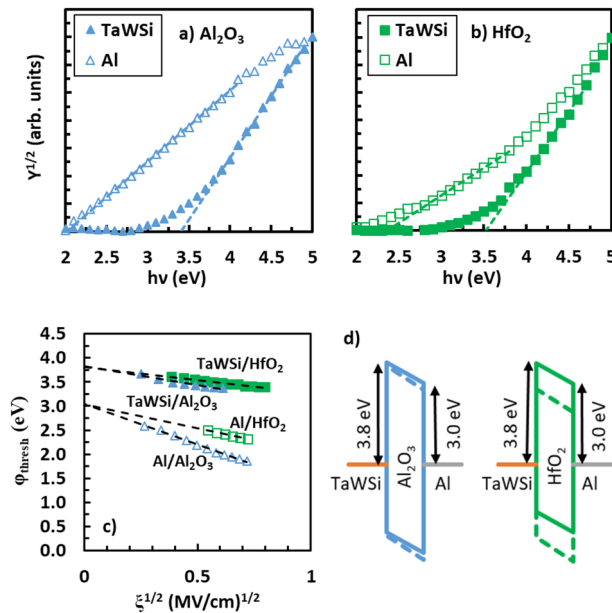


FIG. 4. Representative plots of $Y^{1/2}$ vs. $h\nu$ for (a) Al_2O_3 and (b) HfO_2 in MIM devices with Al top electrodes and TaWSi bottom electrodes, where the dashed lines show the linear φ_{thresh} extraction for each interface. Each plot shown was taken at an applied field in the range of 0.4 to 0.7 MV^2/cm^2 . (c) Schottky plots of φ_{thresh} vs. $\xi^{1/2}$ used to extrapolate the φ_{Bn} from IPE-derived spectral thresholds for the indicated interface, and (d) the IPE based (solid lines) vs. ideal (dashed lines) band diagrams.

electrodes and ZrCuAlNi bottom electrodes (which do not contain Ta), both TaO_x and Al_2O_3 ILs can be ruled out as the major source of tailing. Charge in the dielectric seems the most likely explanation as lateral charge non-uniformities can cause IPE threshold tailing. As previously discussed, Au^+ charge in the insulator may also be responsible for the reduction of the barrier height in the Au top electrode devices. In addition, charge at the interface can reduce influence of electric field on the barrier height.¹⁸

The φ_{Bn} values for each insulator are listed in Table II. In Fig. 4(d), energy band diagrams of the Al top gate devices based on the experimentally determined φ_{Bn} values from Table II (solid lines) are superimposed on band diagrams predicted by $\varphi_{\text{Bn}} = \Phi_{\text{M}} - \chi_{\text{I}}$ (dashed lines). We find much larger (~ 0.7 – 0.8 eV) TaWSi/insulator barriers than for Au top electrode devices, suggesting that Au^+ ion migration may indeed play a role in reducing opposing electrode barrier heights.

The Al top gate TaWSi/ Al_2O_3 φ_{Bn} (3.8 eV) is within error equivalent to that predicted by the ideal Schottky model. The TaWSi/ HfO_2 φ_{Bn} , on the other hand, is higher than the Schottky model prediction by about 0.9 eV. For HfO_2 , the φ_{Bn} increase over the ideal model for both TaWSi bottom and Al top electrodes is similar, with an approximately 0.8–0.9 eV increase. This points to a negative fixed charge in the HfO_2 or perhaps the formation of an Al_2O_3 IL at the top Al electrode. Comparing the Al with the Au top electrode devices, it is seen that the Al/insulator barrier heights are smaller than the Au/insulator barrier heights for all insulators. For both HfO_2 and Al_2O_3 , this difference is roughly equal to the expected $\Phi_{\text{M,vac}}$ difference between Au and Al ($\Delta\Phi_{\text{Au-Al}} \sim 0.9$ eV). Comparing to our previous work with a ZrCuAlNi bottom electrode, the Al/insulator barrier heights are equal, within experimental error.¹⁴ The TaWSi barriers are 0.8 eV and 0.6 eV greater than that measured for ZrCuAlNi with Al_2O_3 and HfO_2 , respectively,¹⁴ confirming that TaWSi has a larger effective work-function than ZrCuAlNi.

Finally, the goal of this work is to use IPE to directly measure metal/insulator φ_{Bn} 's in a device stack so as to be able to better predict device behavior. For high quality ALD Al_2O_3 , thick enough so that conduction is not dominated by direct tunneling, and moderate to high Φ_{M} electrodes, Fowler-Nordheim tunneling (FNT) dominates conduction. The onset of FNT appears as a distinct “knee” in the current density vs. voltage curve, at a voltage dependent on φ_{Bn} of the

TABLE II. Barrier heights extracted from devices in this work with Al top electrodes, compared to literature values for the respected Al barrier height. Measured barrier heights are given with an expected error of ± 0.1 eV.

Insulator (χ_{I})	Measured φ_{Bn} (± 0.1 eV)		Literature $\varphi_{\text{Bn,Al}}$ (eV)
	TaWSi	Al	
Al_2O_3 (1.4 eV ³⁴)	3.8	3.0	2.9 ³⁰
HfO_2 (2.25 eV ³⁵)	3.8	3.0	2.5 ³¹

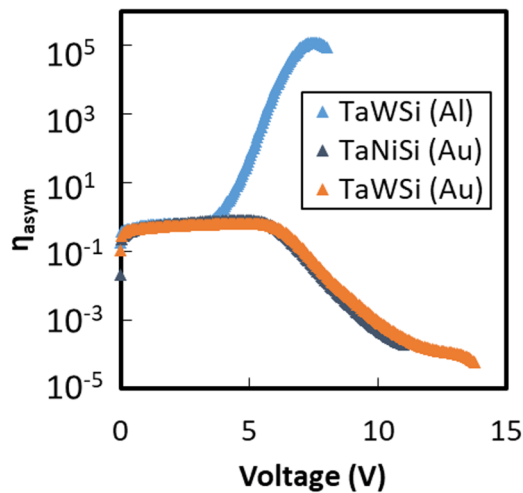


FIG. 5. Voltage vs. current asymmetry for Al_2O_3 MIM devices with the indicated bottom (top) electrodes.

electrode opposite the injecting electrode and the thickness of the insulator. Above the knee, the magnitude of conduction with the bottom electrode held at ground and positive (negative) bias applied to the top electrode depends inversely on $\varphi_{\text{Bn,bottom}}$ ($\varphi_{\text{Bn,top}}$). In other words, the greater the conduction, the smaller the barrier height at the injecting electrode. Therefore, by looking at asymmetry, defined here as the negative bias current over the positive bias current at the same absolute voltage ($\eta_{\text{asym}} = I^-/I^+$), the relative size of the barriers may be assessed. $\eta_{\text{asym}} > 1$ indicates that the barrier height of the top electrode is less than the bottom electrode, $\varphi_{\text{Bn,top}} < \varphi_{\text{Bn,bottom}}$, meaning $\Phi_{\text{eff,top}} < \Phi_{\text{eff,bottom}}$ and $\eta_{\text{asym}} < 1$ indicates that $\Phi_{\text{eff,top}} > \Phi_{\text{eff,bottom}}$. Shown in Fig. 5 are plots of η_{asym} vs. voltage for Al_2O_3 MIM devices with either TaWSi or TaNiSi amorphous metal bottom electrodes and either Au or Al top electrodes. For TaWSi bottom electrode devices, $\eta_{\text{asym}} > 1$ for an Al top electrode and $\eta_{\text{asym}} < 1$ for a Au top electrode, indicating that $\Phi_{\text{eff,Al}} < \Phi_{\text{eff,TaWSi}} < \Phi_{\text{eff,Au}}$ and that $\varphi_{\text{Bn,Al}} < \varphi_{\text{Bn,TaWSi}} < \varphi_{\text{Bn,Au}}$. $\eta_{\text{asym}} < 1$ is also seen for the TaNiSi/ Al_2O_3 /Au device. These results are inconsistent with ideal Schottky model predictions, but consistent with our IPE measurements which show $\Delta\varphi_{\text{Bn,TaWSi-Au}} = -1.0$ eV, $\Delta\varphi_{\text{Bn,TaWSi-Al}} = +0.8$ eV, and $\Delta\varphi_{\text{Bn,TaNiSi-Au}} = -0.6$ eV.

IV. SUMMARY/CONCLUSION

The electron energy barrier heights between two recently reported Ta-based amorphous metals (TaWSi and TaNiSi), TaN, and ALD Al_2O_3 and HfO_2 insulators with Al top electrodes are measured experimentally using internal photoemission (IPE) spectroscopy. A comparison is also made between Al and Au top electrodes for devices with a TaWSi bottom electrode. The measured barrier heights for both the Al and Au top electrodes are near the Schottky model values ($\varphi_{\text{Bn}} = \Phi_{\text{M}} - \chi$) and

consistent with previous IPE reports for each insulator. For the Ta-based metal bottom electrodes with Al_2O_3 , φ_{Bn} increases with increasing Φ_{M} : $\varphi_{\text{Bn}} = 2.9, 3.1,$ and 3.3 eV for TaN, TaWSi, and TaNiSi, respectively. For HfO_2 , however, the barrier heights are relatively independent of Φ_{M} : $\varphi_{\text{Bn,TaNiSi}} \approx \varphi_{\text{Bn,TaWSi}} \approx \varphi_{\text{Bn,TaN}} \approx 3.0$ eV. The difference between HfO_2 and Al_2O_3 is attributed to enhanced Fermi-level pinning due to a larger dielectric constant—confirmed by the slope parameter, S , which was found to be 0.89 and 0.44–0.69 for Al_2O_3 and HfO_2 , respectively. In devices with a TaWSi bottom electrode, an Au top electrode leads to significantly lower barrier heights than were obtained with Al, 0.6 eV and 0.8 eV lower for HfO_2 and Al_2O_3 , respectively. Measurements of the current-voltage asymmetry of MIM diodes are consistent with the IPE measured barriers, whereas the asymmetry is inconsistent with the Schottky model predictions of barrier heights.

A comparison to previous work with amorphous ZrCuAlNi bottom and Al top electrodes indicates that the electron barriers for TaWSi with HfO_2 and Al_2O_3 are 0.8 eV and 0.6 eV greater, respectively, than the same barriers with ZrCuAlNi. This confirms that for Al_2O_3 , TaWSi has a larger effective work function than ZrCuAlNi, ~ 5.2 eV vs. ~ 4.7 eV, respectively.¹⁴ Combined with low roughness and significantly higher temperature stability than ZrCuAlNi (greater than 900°C vs. less than 400°C), TaWSi appears promising for use as a high work function bottom electrode in MIM device applications.

ACKNOWLEDGMENTS

This work was supported by NSF Center for Sustainable Materials Chemistry, Grant No. CHE-1606982. The authors thank C. Tasker for equipment support and T. Klarr (now at Micron, Boise, ID) for device fabrication assistance. Part of this work was conducted at the Materials Synthesis and Characterization (MaSC) Center, a National Nanotechnology Coordinated Infrastructure (NNCI) Northwest Nanotechnology Infrastructure (NWNII) user facility at Oregon State University, which is supported in part by the National Science Foundation (NSF) (Grant No. ECC-1542101) and Oregon State University.

REFERENCES

- A. Sharma, V. Singh, T. L. Bougher, and B. A. Cola, *Nat. Nanotechnol.* **10**, 1027 (2015).
- M. Bareib, B. N. Tiwari, A. Hochmeister, G. Jegert, U. Zschieschang, H. Klauk, B. Fabel, G. Scarpa, G. Koblmüller, G. H. Bernstein, W. Porod, and P. Lugli, *IEEE Trans. Microw. Theory Tech.* **59**, 2751 (2011).
- G. Moddel and S. Grover, *Rectenna Solar Cells* (Springer Science & Business Media, New York, 2013).
- M. Heiblum, *Solid-State Electron.* **24**, 343 (1981).
- S. Vaziri, A. D. Smith, M. Östling, G. Lupina, J. Dabrowski, G. Lippert, W. Mehr, F. Driussi, S. Venica, V. Di Lecce, A. Gnudi, M. König, G. Ruhl, M. Belete, and M. C. Lemme, *Solid State Commun.* **224**, 64 (2015).
- G. Karbasian, M. S. McConnell, H. George, L. C. Schneider, M. J. Filmer, A. O. Orlov, A. N. Nazarov, and G. L. Snider, *Appl. Sci.* **7**, 246 (2017).
- H.-S. P. Wong, H.-Y. Lee, S. Yu, Y.-S. Chen, Y. Wu, P.-S. Chen, B. Lee, F. T. Chen, and M.-J. Tsai, *Proc. IEEE* **100**, 1951 (2012).
- D. Z. Austin, K. E. K. Holden, J. Hinz, and J. F. Conley, Jr., *Appl. Phys. Lett.* **110**, 263503 (2017).

- ⁹N. Alimardani, S. W. King, B. L. French, C. Tan, B. P. Lampert, and J. F. Conley, Jr., *J. Appl. Phys.* **116**, 024508 (2014).
- ¹⁰N. Alimardani, E. W. Cowell, J. F. Wager, J. F. Conley, Jr., D. R. Evans, M. Chin, S. J. Kilpatrick, and M. Dubey, *J. Vac. Sci. Technol. A* **30**, 01A113 (2012).
- ¹¹A. A. Khan, G. Jayaswal, F. A. Gahaffar, and A. Shamim, *Microelectron. Eng.* **181**, 34 (2017).
- ¹²E. W. Cowell, N. Alimardani, C. C. Knutson, J. F. Conley, Jr., D. A. Keszler, B. J. Gibbons, and J. F. Wager, *Adv. Mater.* **23**, 74 (2011).
- ¹³N. Alimardani and J. F. Conley, Jr., *Appl. Phys. Lett.* **105**, 082902 (2014).
- ¹⁴M. A. Jenkins, T. Klarr, D. Z. Austin, W. Li, N. V. Nguyen, and J. F. Conley, Jr., *Phys. Status Solidi RRL – Rapid Res. Lett.* **12**, 1700437 (2018).
- ¹⁵J. M. McGlone, K. R. Olsen, W. F. Stickle, J. E. Abbott, R. A. Pugliese, G. S. Long, D. A. Keszler, and J. F. Wager, *MRS Commun.* **7**, 715 (2017).
- ¹⁶J. M. McGlone, K. R. Olsen, W. F. Stickle, J. E. Abbott, R. A. Pugliese, G. S. Long, D. A. Keszler, and J. F. Wager, *J. Alloys Compd.* **650**, 102 (2015).
- ¹⁷V. Afanas'ev, N. Kolomiets, M. Houssa, and A. Stesmans, *Phys. Status Solidi A*, **215**, 1700865 (2017).
- ¹⁸V. V. Afanas'ev and A. Stesmans, *J. Appl. Phys.* **102**, 081301 (2007).
- ¹⁹J. Tersoff, *Phys. Rev. Lett.* **52**, 465 (1984).
- ²⁰W. Mönch, *Phys. Rev. Lett.* **58**, 1260 (1987).
- ²¹Y.-C. Yeo, T.-J. King, and C. Hu, *J. Appl. Phys.* **92**, 7266 (2002).
- ²²V. K. Adamchuk and V. V. Afanas'ev, *Prog. Surf. Sci.* **41**, 111 (1992).
- ²³N. V. Nguyen, O. A. Kirillov, W. Jiang, J. E. Maslar, W. Kimes, and J. S. Suehle, *ECS Trans.* **13**, 161 (2008).
- ²⁴V. V. Afanas'ev, A. Stesmans, L. Pantisano, S. Cimino, C. Adelman, L. Goux, Y. Y. Chen, J. A. Kittl, D. Wouters, and M. Jurczak, *Appl. Phys. Lett.* **98**, 132901 (2011).
- ²⁵W. Ludwig and B. Korneffel, *Phys. Status Solidi B* **24**, K137 (1967).
- ²⁶K. H. Gundlach and J. Kadlec, *Thin Solid Films* **28**, 107 (1975).
- ²⁷J. Kadlec and K. H. Gundlach, *Phys. Status Solidi A* **37**, 11 (1976).
- ²⁸N. V. Nguyen, O. Kirillov, H. D. Xiong, and J. S. Suehle, in *AIP Conf. Proc.* (AIP Publishing, 2007), pp. 308–314.
- ²⁹V. V. Afanas'ev, *Internal Photoemission Spectroscopy: Fundamentals and Recent Advances* (Elsevier, 2014).
- ³⁰V. V. Afanas'ev, M. Houssa, A. Stesmans, and M. M. Heyns, *J. Appl. Phys.* **91**, 3079 (2002).
- ³¹V. V. Afanas'ev, A. Stesmans, F. Chen, X. Shi, and S. A. Campbell, *Appl. Phys. Lett.* **81**, 1053 (2002).
- ³²J. Widiez, K. Kita, K. Tomida, T. Nishimura, and A. Toriumi, *Jpn. J. Appl. Phys.* **47**, 2410 (2008).
- ³³M. A. Jenkins, T. Klarr, J. M. McGlone, J. F. Wager, and J. F. Conley, Jr., *ECS Trans.* **85**, 729 (2018).
- ³⁴S. Swaminathan, Y. Sun, P. Pianetta, and P. C. McIntyre, *J. Appl. Phys.* **110**, 094105 (2011).
- ³⁵S. Monaghan, P. K. Hurley, K. Cherkaoui, M. A. Negara, and A. Schenk, *Solid-State Electron.* **53**, 438 (2009).
- ³⁶J. M. McGlone, "Thermally-Stable Amorphous Metal Thin Films," Masters Thesis (Oregon State University, 2014).
- ³⁷J. Robertson, *J. Vac. Sci. Technol. B* **18**, 1785 (2000).
- ³⁸S. B. Samavedam, L. B. La, P. J. Tobin, B. White, C. Hobbs, L. R. C. Fonseca, A. A. Demkov, J. Schaeffer, E. Luckowski, A. Martinez, M. Raymond, D. Triyoso, D. Roan, V. Dhandapani, R. Garcia, S. G. H. Anderson, K. Moore, H. H. Tseng, C. Capasso, O. Adetutu, D. C. Gilmer, W. J. Taylor, R. Hegde, and J. Grant, in *IEEE International Electron Devices Meeting 2003. IEDM 03 Technical Digest* (IEEE, 2003), pp. 13.1.1–13.1.4.
- ³⁹J. F. Wager and K. Kuhn, *Crit. Rev. Solid State Mater. Sci.* **42**, 373 (2017).
- ⁴⁰X. Qin and R. M. Wallace, *Appl. Phys. Lett.* **107**, 081608 (2015).
- ⁴¹P. M. Lenahan and J. F. Conley, Jr., *J. Vac. Sci. Technol. B* **16**, 2134 (1998).
- ⁴²L. Pantisano, V. V. Afanas'ev, S. Cimino, C. Adelman, L. Goux, Y. Y. Chen, J. A. Kittl, D. Wouters, and M. Jurczak, *Microelectron. Eng.* **88**, 1251 (2011).
- ⁴³R. J. Powell, *J. Appl. Phys.* **40**, 5093 (1969).
- ⁴⁴S. Shamulilia, V. V. Afanas'ev, A. Stesmans, T. Schram, and L. Pantisano, *J. Appl. Phys.* **104**, 073722 (2008).
- ⁴⁵J. G. Simmons and R. R. Verderber, *Proc. R. Soc. Lond. A* **301**, 77 (1967).
- ⁴⁶C.-N. Peng, C.-W. Wang, T.-C. Chan, W.-Y. Chang, Y.-C. Wang, H.-W. Tsai, W.-W. Wu, L.-J. Chen, and Y.-L. Chueh, *Nanoscale Res. Lett.* **7**, 559 (2012).
- ⁴⁷M. He and T.-M. Lu, *Metal-Dielectric Interfaces in Gigascale Electronics: Thermal and Electrical Stability* (Springer, New York, 2012).